Laser-induced field emission from a tungsten nanotip by circularly polarized femtosecond laser pulses

Hirofumi Yanagisawa,[1,*] Thomas Greber,[2] Christian Hafner,[3] and Juerg Osterwalder[2]
[1]*Physics Department, Ludwig-Maximilians-Universitaet Munich, D-85748 Garching, Germany; Max Planck Institute of Quantum Optics, D-85748 Garching, Germany; and Institute for Quantum Electronics, ETH Zurich, CH-8093 Zurich, Switzerland*
[2]*Physik-Institut, Universitaet Zurich, CH-8057 Zurich, Switzerland*
[3]*Institute of Electromagnetic Fields, ETH Zurich, CH-8092 Zurich, Switzerland*

(Received 4 October 2019; revised manuscript received 1 December 2019; published 8 January 2020)

We have investigated emission patterns and energy spectra of electrons from a tungsten nanotip induced by circularly polarized femtosecond laser pulses. Variations of emission patterns were observed for different helicities of circular polarization while the energy spectra remained almost identical. The physics behind this difference in emission patterns is the change in propagation directions of surface electromagnetic waves on the tip apex. The energy spectra showed the same spectroscopic signatures as the linearly polarized laser in a strong-field regime, which are a low-energy peak and a plateau feature. The low-energy peak is due to a delayed electron emission with respect to a prompt emission. The experimental data and plasmonic simulations support our previous conclusion, where the observed delayed emission processes originate from an inelastic rescattering process. This work demonstrates that the use of circular polarization is an easy means to add extra knobs to control the spatial and temporal emission from a nanotip at the nanometer and femtosecond scale. It could find applications as a helicity-driven subcycle optical switch.

DOI: 10.1103/PhysRevB.101.045406

I. INTRODUCTION

Femto- and attosecond dynamics of coherent electrons in nano-objects and their nanoscale spatial manipulation using femtosecond laser pulses have been intensively studied in basic and applied research [1–29]. One of the powerful tools for investigating such ultrafast dynamics on a nanoscale is laser-induced field emission microscopy [6–10]. Applying a high voltage on a metallic tip with nanometer sharpness (a nanotip) induces strong electric fields only at the apex. The strong fields bend the surface potential barrier at the apex and lead to electron tunneling from the solid to the vacuum, which is called field emission [30]. The field emission propagates radially from the tip apex because of strong dc fields being radially directed around the apex. As a result, the emitted electrons magnify nanoscale geometrical information on the apex to a macroscopic scale, which enables field emission microcopy (FEM) [30]. Illuminating such a nanotip with femtosecond laser pulses generates pulsed field emission from nanoscale areas [6], which in turn realizes laser-induced field emission microscopy (LFEM).

By performing LFEM together with spectroscopic experiments, previous works revealed intriguing atto- to femtosecond electron dynamics within nanometer areas, such as plasmonic effects [6–13,27], ultrafast coherent electron emission [10,11], femtosecond photoexcitation dynamics [9,14–16], heating effects [16,17], optical tunneling emission [18–29], ultrafast rectification effects [22], attosecond near-field sampling [25,26], elastic and inelastic rescattering processes [19,23,24,26], and subcycle emission [20,22,28]. In particular, plasmonic effects play a central role in the laser-induced electron emission from a nanotip because they create nanoscale optical fields on the tip apex [6]. Furthermore, plasmonic effects create an asymmetric local electric field distribution on the tip apex as schematically shown in Fig. 1(a), and subsequently induce asymmetric electron emission [7–10]. As a result, an ultrafast pulsed coherent electron source with emission site selectivity on a scale of a few tens of nanometers has been realized [10]. The field emission from a nanotip is most often used as a coherent electron source for electron microscopy [31,32] or in vacuum nanoelectronics [33]. The laser-induced field emission provides a conventional electron source with new degrees of spatiotemporal freedom on scales of nanometers and femtoseconds. This kind of electron source can be used for time-resolved electron microscopy [34,35] or ultrafast devices [36]. For such applications, emission mechanisms and their ultrafast dynamics have been studied for a wide range of laser intensity by measuring their electron energy spectra.

In the weak laser field regime, a laser pulse excites electrons by the absorption of single or multiple photons. The photoexcited electrons are then emitted into a vacuum either through the potential barrier or over the barrier [6–16]. In the strong-field regime, in addition to the photoexcitation, the laser field modifies the surface potential barrier and causes tunneling emission [18–29]. Once in the vacuum, the emitted electrons experience acceleration and deceleration due to the

*hirofumi.yanagisawa@mpq.mpg.de

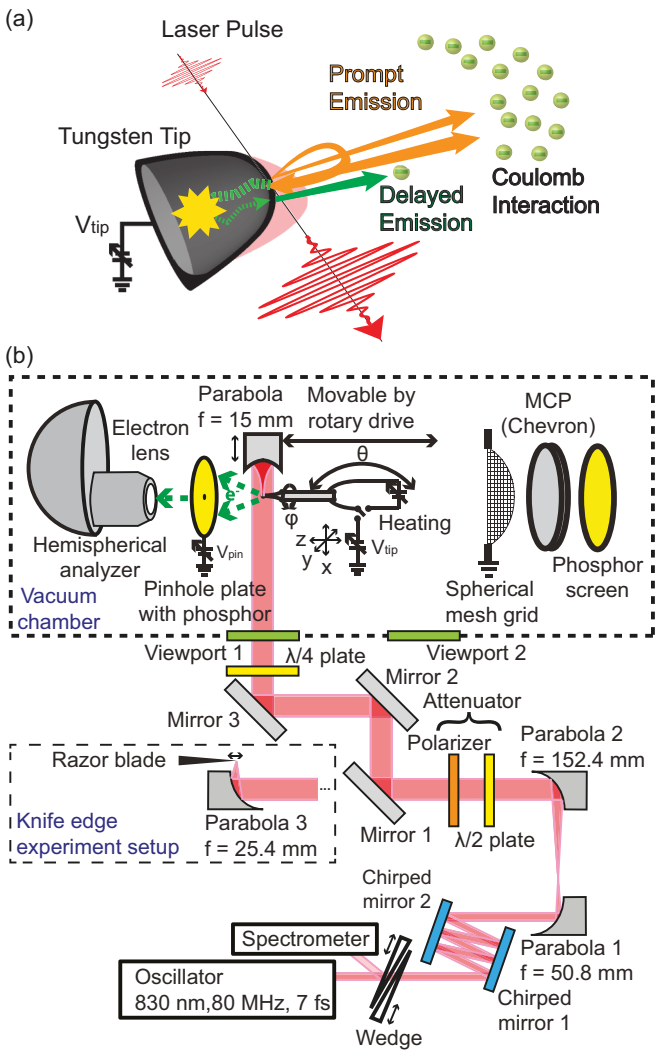

FIG. 1. (a) A conceptual diagram of electron dynamics in the strong-field regime. Different emission processes under strong fields are indicated by the orange and green arrows. (b) A schematic diagram of our experimental setup. See the text for details.

oscillating laser field. Some of the electrons are driven back to the tip and elastically rescatter from the surface (elastic rescattering emission) [19,23,26], while other electrons are emitted without rescattering (direct emission). These processes are depicted by the orange arrows in Fig. 1(a); we refer to them as *prompt emission*. Furthermore, upon rescattering, some of these electrons can even enter the tip and be emitted after experiencing inelastic scattering in the solid (inelastic rescattering emission) as indicated by the green arrows in Fig. 1(a) [24]. Since this process induces a delay of tens of femtoseconds with respect to the prompt emission, it is called delayed emission. The delayed emission has been previously discussed along with thermal emission because it also causes a delayed emission. Our spectroscopic experiments, together with extensive simulations, indicated that delayed emission is mainly driven by the inelastic rescattering [24].

The experiments discussed above were all done with linearly polarized laser pulses. Further investigations of plasmonic responses and ultrafast electron dynamics induced by circularly polarized light are expected to explore further functionalities of laser-induced field emission. Here, we investigate the LFEM images, namely, the emission patterns, and the energy spectra of electrons from a tungsten nanotip induced by circularly polarized light with different helicities. The LFEM images showed a change of emission sites with helicity, which could be successfully explained by the physics of the emission site selectivity due to plasmonic effects. In contrast to the LFEM images, the energy spectra did not show any helicity dependence. The spectra reproduced the signature of the delayed emission as we observed it with linearly polarized light. The signal level of the delayed emission, however, was reduced to half compared with that of the linear polarization for the same laser fluence. When performing plasmonic simulations, we found that the observed signal reduction offers additional evidence that the delayed emission is driven by the inelastic rescattering process.

This manuscript consists of four sections. In Sec. II, we will explain our experimental setup. In Sec. III A, we will present LFEM images and discuss plasmonic responses of a nanotip for circularly polarized light with different helicities. In Sec. III B, we show measured energy spectra and discuss the delayed emission process in the strong-field regime. In the last section, we present conclusions.

II. METHODOLOGY

Figure 1(b) shows a schematic diagram of our optical system together with the vacuum system, which is the same setup as used in our previous work [24]. An oscillator generates 7-fs laser pulses (center wavelength: 830 nm; repetition rate: 80 MHz). The circularly polarized light pulses are generated using a $\lambda/4$ plate placed right before the view port of the vacuum chamber. A pair of chirped mirrors is used for dispersion compensation. The positions of the glass wedges were optimized in such a way that the electron intensity from the tip was maximized. We confirmed that the pulse width can reach 7 fs using spectral phase interferometry for direct electric-field reconstruction (SPIDER). The circularly polarized light is typically slightly elliptic. The ellipticities were obtained by measuring laser fields, F, as a function of angle around the propagation axis. The ellipticity is defined as $F_{\min}/F_{\max}$. The laser fields, F, were obtained from the measured power of the laser passing through an additional polarizer plate that is placed after the $\lambda/4$ plate [not shown in Fig. 1(b)]. Here, the ellipticity of the right-handed circularly polarized laser was 97.5% and that of the left-handed one was 93.5%. Note that the polarization vectors of the left- (right-) handed laser pulses rotate counterclockwise (clockwise) when one looks along the propagation direction of the pulses.

The laser beam is introduced into the vacuum chamber (base pressure: 9×10^{-11} mbar). In the vacuum chamber, a parabolic mirror focuses the laser onto the apex of a tungsten tip. The parabolic mirror is movable along the x axis. Outside of the chamber, the laser beam is expanded by a pair of parabolic mirrors 1 and 2 for creating a tightly focused beam. The positions of the two parabolas are adjusted to have a minimum beam waist at the focus of parabola 3. The beam waist was measured by a knife edge experiment [37], and from this measurement, the beam waist at the tip apex is

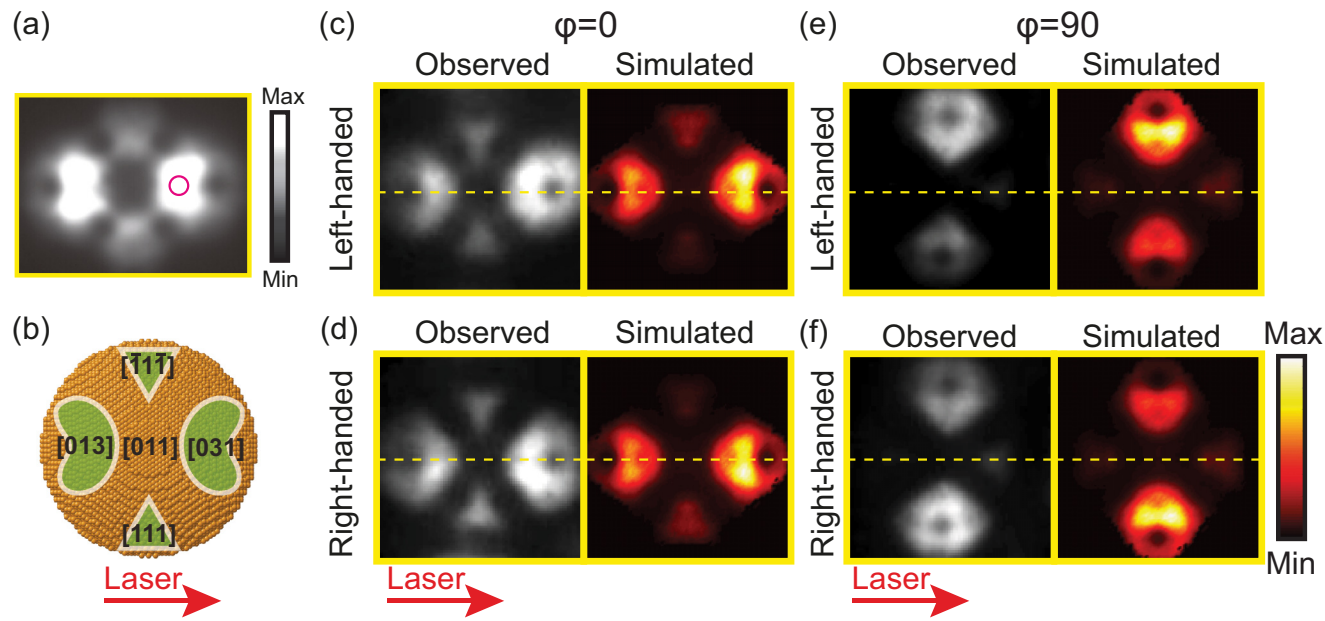

FIG. 2. (a) Electron emission patterns from a tungsten nanotip oriented towards the [011] direction without laser illumination. Tip voltage V_{tip} was −2800 V. (b) The front view of the atomic structure of a tip apex based on a ball model. The green areas correspond to the electron emission area. (c–f) Experimentally observed (left) and simulated (right) electron emission patterns from a nanotip induced by circularly polarized laser pulses. In all images, V_{tip} was −1900 V and the laser fluence was 1.22 mJ/cm^2. The simulations were performed using the same code as we used previously [7,8]. In all the pictures, the laser propagation direction is the same and is indicated by red arrows.

estimated to be approximately 3.5 μm in diameter. The tip is mounted on a five-axis piezo stage controlling x, y, z, θ, and φ. Thus the tip apex can be precisely positioned into the focus of the laser. The apex of the tungsten tip is crystallized and oriented towards the [011] direction; its radius of curvature is approximately 100 nm [7,8].

To perform LFEM and spectroscopic experiments, there are two types of detectors in the vacuum chamber as shown in Fig. 1(b); one is a two-dimensional detector (OCI-LEED) and the other one is a hemispherical energy analyzer (VG CLAM2). To change the detectors, the tip is rotated 180° in the θ direction and the parabolic mirror is moved to the other side. The two-dimensional detector was used to observe the electron emission patterns from the tip. Cleanliness of the tip apex can be assessed from the emission patterns [38]. The typical FEM pattern from a clean tungsten tip apex is shown in Fig. 2(a). The intensity distribution of the electron emission is mainly dependent on the distribution of the local work function on the apex [7,8]. The most intense emission can be observed around the lowest work function area, namely, a [310] type facet as schematically drawn in Fig. 2(b). The clean surface was prepared by heating the tip. Since the tip apex can be quickly contaminated even under ultrahigh vacuum, all the measurements were done within 15 min after the sample heating. In the laser experiments, the laser will propagate from left to right in the FEM image as indicated by the red arrows in Fig. 2.

The electron analyzer is used to measure energy spectra of the electrons emitted from the tip apex. A pinhole plate covered with phosphor was mounted between the tip and the analyzer in order to observe emission patterns and to define a particular emission site to be measured. The pinhole of the energy analyzer was positioned on the [310] type facet, and its position and relative diameter are roughly indicated by a red circle in Fig. 2(a). This condition is the same as in our previous study with linearly polarized laser pulses. The diameter of the pinhole is 2 mm and the distance between the pinhole plate and the tip apex is 13 mm. Excellent performance of the analyzer system in terms of energy resolution was already demonstrated in our previous work [9,15,24]. Note that we used exactly the same sample as we used in our previous work with linearly polarized light.

III. RESULTS AND DISCUSSION

A. Plasmonic responses under circularly polarized light

In this section, we discuss the plasmonic response of a nanotip to the circularly polarized light based on the LFEM experiments. The left panels of Figs. 2(c)–2(f) show the observed electron emission patterns induced by the left- and right-handed circularly polarized laser for two different tip azimuthal angles. We notice two characteristics. Firstly, the observed LFEM images become asymmetric compared to the FEM image in Fig. 2(a). Secondly, the LFEM images change for different helicities. In the case of the left-handed polarization, the emission patterns become strongest around the upper right area in Figs. 2(c) and 2(e). In contrast, the emission patterns become strongest around the lower right area in Figs. 2(d) and 2(f). Our previous work revealed that such asymmetric emission originates from the asymmetric optical field distributions on the tip apex [7,8].

Here, we confirm the same physics by performing the following simulation. First, the plasmonic response of the tip apex was simulated by solving Maxwell equations using the OPENMAXWELL package [39]. A dropletlike shape was

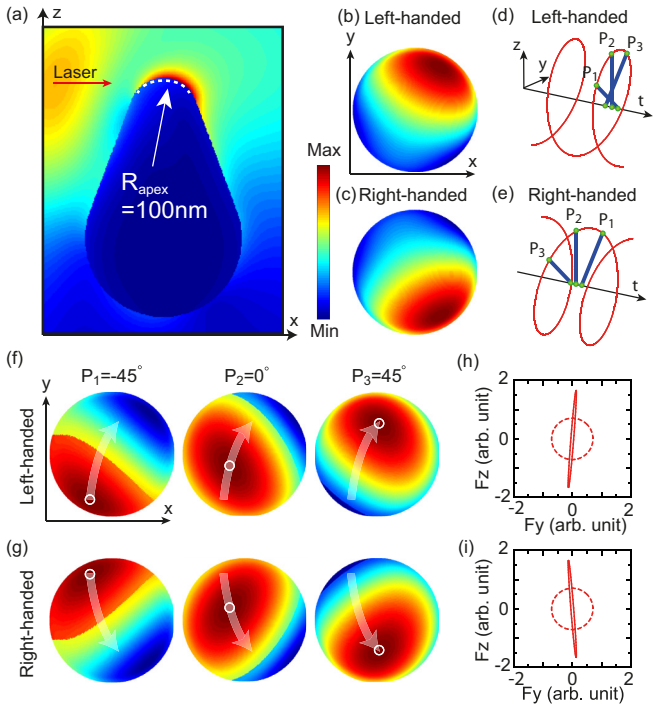

FIG. 3. (a) The model tip used for the plasmonic simulations. In (b,c), the front views of the time-averaged field distributions at the tip apex are given for left-handed and right-handed circularly polarized laser pulses, respectively. The view area is indicated by the white dashed line in (a). (d,e) Schematic diagrams of the variation of optical fields over time for left-handed and right-handed circularly polarized laser light, respectively. (f,g) show the transient optical field distributions on the tip apex (front views of the model tip) at the phases given in (d,e). The white arrows indicate the propagation of the maximum optical fields. (h,i) indicate the traces of the location of maximum field strength of optical field vectors at the very top of the tip apex for a single optical cycle of the left-handed and the right-handed polarized laser pulses, respectively. The solid lines and dashed lines are with and without the presence of the nanotip, respectively. The fields are projected onto the $y-z$ plane.

employed as a model tip as shown in Fig. 3(a). The radius of curvature of the tip apex is 100 nm. In the simulations, we only used a continuous wave with a wavelength of 800 nm because the optical field distribution does not change significantly, even for a laser pulse with a broad band spectrum [16,24]. The laser is propagating along the x direction as indicated by a red arrow, and is focused to a 1 μm waist (diameter) at the tip's apex. The dielectric function ε of tungsten at 800 nm was employed: a real part $\mathrm{Re}(\varepsilon) = 5.2$ and an imaginary part $\mathrm{Im}(\varepsilon) = 19.4$ [40]. A circularly polarized laser beam was generated by combining two linear polarizations, namely, vertical and horizontal, with relative phase shifts of $+\pi/2$ or $-\pi/2$ for different helicities [41]. The resulting time-averaged local electric field distributions on the tip apex are shown in Figs. 3(b) and 3(c) for the left- and right-handed polarization, respectively. They are the front views of the model tip, where the view area is highlighted by a dashed curve in Fig. 3(a). The simulated distributions show that the maximum field is situated on the upper right in the case of the left-handed circular polarization and that it moves to the lower right for the right-handed one. This is consistent with our observations in Figs. 2(c)–2(f).

Next, using the simulated local electric field distribution, we have reproduced LFEM images based on the Fowler-Nordheim theory. In the experiments, the LFEM images were taken with a laser of weak intensity [7–9,15]. Hence, we assumed a model for the weak-field regime. The details are described in Refs. [7,8]. The laser-induced field emission current depends on work function, dc fields, and laser intensity on the apex. The work function map was determined from the observed FEM image [7,8]. The dc field distribution on the tip apex was obtained by using OPENMAXWELL [7,8], and the dc field is 2.3 V/nm at the very top of the tip apex, which is taken from Ref. [10]. The laser intensity was adjusted by a parameter, S_1, which is the occupation number of the time-averaged electron distribution function for one-photon excitation [7]. S_1 is proportional to the laser fluence. In our previous work with linearly polarized light, S_1 was 1.6×10^{-6} for the fluence of 2.44 mJ/cm^2, while the fluence of circularly polarized light in this experiment was half of that, i.e., 1.22 mJ/cm^2. As discussed later, the laser intensity of circular polarization at the tip apex will be half that of the linear polarization for the same fluence. Hence, here we set $S_1 = 0.4 \times 10^{-6}$. The resulting patterns are shown in the right panels of Figs. 2(c)–2(f). There is good agreement between the experimental and simulated data, which led us to conclude that the modulation of local electric field distributions is responsible for the changes in the emission patterns.

The simulations further reveal that the local electric field distributions vary because surface electromagnetic waves propagate in different directions. Surface electromagnetic waves are the waves that result from the coupling of the surface charges and the electromagnetic wave such as in a surface plasmon polariton. Surface electromagnetic waves are classified in terms of the dielectric functions of the interacting material [42], and strictly speaking, the excited surface electromagnetic waves on tungsten are Zenneck waves as discussed in Refs. [7,8]. The resulting field distributions on the tip apex are due to the interference of the excited surface electromagnetic waves [7,8]. In Figs. 3(f) and 3(g), we show how the local electric field distribution evolves over subcycle time steps for the left-handed and right-handed polarizations, respectively. Their phases are visualized in Figs. 3(d) and 3(e), respectively. As denoted by the white arrows in Figs. 3(f) and 3(g), the surface electromagnetic waves move upwards for the left-handed polarization, and downwards for the right-handed one. (See Video 1 in the Supplemental Material [43] for the temporal evolution of local electric field distributions for one optical cycle.) This difference results in the variation shown in Figs. 3(b) and 3(c). It should also be noted that the fields of the surface electromagnetic wave do not preserve the circular polarization. Figures 3(h) and 3(i) indicate the trace of the electric field vectors at the very top of the apex during one optical cycle, which are projected onto the $y-z$ plane. Without the presence of the tip, the field traces are essentially circular as indicated by the dashed lines. In contrast, with a tip, they become elongated along the vertical axis and behave more closely to those in a linearly polarized laser pulse. It should be mentioned that polarization largely affects the electron motion after the emission in the strong laser field regime. For instance,

in the case of gas-phase targets, rescattering processes are mostly suppressed under illumination by circularly polarized light because the liberated electrons do not return to the parent ion [44,45]. In the case of a nanotip, however, the electron dynamics under the circularly polarized light are expected to be similar to that under linearly polarized light according to the above simulations. These dynamics will be discussed in the next section.

B. Electron dynamics in strong-field regime under circularly polarized light

In this section, ultrafast electron dynamics, especially the delayed emission channel in the strong-field regime, will be discussed in relation to energy spectra. In this spectroscopic experiment, the laser fluence is 10 times higher than that in the previous section to be in the strong-field regime. In addition, in order to clearly observe the delayed emission, we worked on a regime where multiple electrons can be generated in a single pulse. In this regime, the prompt emission becomes very dense in both time and space as schematically depicted in Fig. 1(a). Electrons emitted within this charge cloud are decelerated and accelerated by the strong mutual Coulomb interaction (a phenomenon known as space charge effects). The strong space charge effects wash away the entire fine details of spectroscopic signatures in the prompt emission that was observed in previous work using low laser fluence with less than one electron per pulse, such as a low-energy peak of direct emission and multiple high-energy peaks due to the elastic rescattering process [19]. As a result, the energy spectra of the prompt emission show a broad plateau. In contrast, the electrons in the delayed emission shown in Fig. 1(a) can avoid the strong space charge effects; it therefore appears as a sharp peak, which clearly distinguishes the delayed emission from the prompt emission [24]. The solid circles in Fig. 4(a) show the resulting energy spectra. They are identical between the left and right panels. The green solid circles are for the left-handed polarization and the red circles are for the right-handed one. We could not find any significant difference between the two spectra. In both spectra, we observed two distinctive features: a low-energy peak feature and a plateau feature with an almost constant intensity. They are the same features as those observed when using the linearly polarized laser pulses [24]. As a reference, the energy spectra of linear polarization are shown by open triangles in the left and right panels of Fig. 4(a) for three different laser fluences. The striking difference is that the signal level of the two features for the two circular polarizations is much weaker than those for the linear polarization at the same laser fluence. [Compare the three spectra taken with a fluence of 12.2 $\mathrm{mJ/cm^2}$ in the left panel of Fig. 4(a).] Both of these differences suggest substantially weaker field amplitudes at the tip apex in the case of circular polarization. More specifically, the signal levels of the peak feature for the circular polarizations are between those at fluences of 6.1 and 7.3 $\mathrm{mJ/cm^2}$ as shown in the right panel of Fig. 4(a).

For a more quantitative analysis, we decomposed the energy spectra into two emission components as shown in Fig. 4(b). Using a Monte Carlo code [24], which also takes the space charge effects into account, we simulated electron trajectories from the tip apex and reproduced the observed energy spectra as shown in the inset of Fig. 4(b) (see the black solid lines). These calculations allowed us to decompose the spectrum into two parts according to the particular emission processes, from which we learned that the low-energy peak consists of the delayed emission (pink solid lines) and the plateau feature consists of the prompt emission, broadly smeared out by the space charge effects (blue solid lines). Here, to decompose the measured spectrum, we assumed an asymmetric shape for the low-energy peak and used a skew Gaussian distribution: $F(x) = a/(b\sqrt{2\pi})$ $\exp(-[(x-c)/b]^2/2)\{1+\mathrm{erf}[d(x-c)/(b\sqrt{2})]\}$. In this formula, erf is the error function, and a, b, c, and d are the parameters, with which intensity, width, position, and skew of the peak can be controlled. The skew Gaussian peak was subtracted from the measured spectra and a plateau

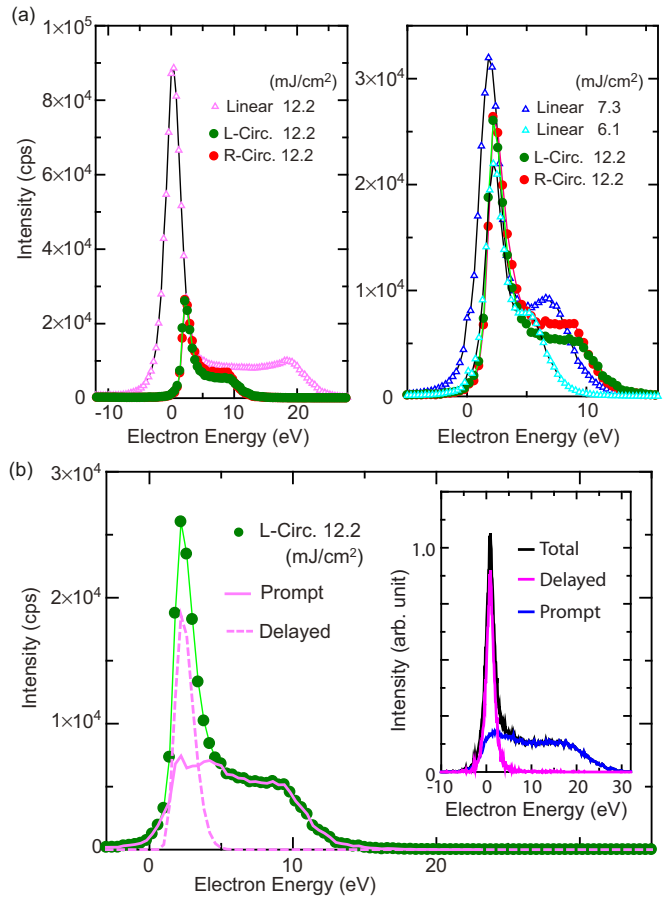

FIG. 4. (a) Measured energy spectra of laser-induced electron emission from a nanotip. The open triangles are the data taken with linearly polarized laser pulses and the solid circles are the data with circularly polarized pulses. The laser fluences are shown in the figure. The data for the two circular polarizations in the left and right panels are identical. (b) The energy spectrum taken by the left-handed circular light (solid circles) together with the decomposed spectra with two different features: a low-energy peak feature (pink dashed lines) and a plateau feature (pink solid lines). The inset shows a simulated energy spectrum in our previous work [24]. It is decomposed into two emission processes: delayed and prompt emissions.

TABLE I. Integrated count rates for the delayed emission process (the low-energy peak feature) and the prompt emission process (the plateau feature) for different laser fluences.

	Peak (counts)	Plateau (counts)
Linear 12.2 mJ/cm^2	2.2×10^5	2.6×10^5
Linear 7.3 mJ/cm^2	4.2×10^4	8.9×10^4
Linear 6.1 mJ/cm^2	2.0×10^4	5.2×10^4
L-Circ. 12.2 mJ/cm^2	3.0×10^4	6.5×10^4
R-Circ. 12.2 mJ/cm^2	3.0×10^4	7.3×10^4

component was obtained. The resulting plateau was compared with the simulated one [see inset of Fig. 4(b)]. The parameters for the skew Gaussian distribution were determined in such a way that the two plateau features from experiment and simulation became similar to each other. The now decomposed low-energy peak and plateau features are shown by dashed and solid pink curves in Fig. 4(b), respectively. Each of them was then integrated, and the values are summarized in Table I. Because the analytical functions for the plateau feature were not available, there is an error of, at most, $\pm 10\%$ in the estimation of the integrated counts. The values in Table I also show that the count rates for circular polarization with the fluence of 12.2 mJ/cm^2 are situated between those for linear polarization with 6.1 and 7.3 mJ/cm^2. By linearly interpolating the count rates of the low-energy peak between 6.1 and 7.3 mJ/cm^2, the count rates for circular polarization turned out to be close to the values for linear polarization with a fluence of around 6.7 mJ/cm^2. Importantly, the following arguments tell us that this reduction of the low-energy peak supports our previous conclusion where the delayed emission is driven by an inelastic rescattering process.

As mentioned in the Introduction, the delayed emission was extensively discussed based on the inelastic rescattering model and the thermal emission model, as the thermal emission also causes a delayed emission [24]. In the current study, our plasmonic simulations revealed that the circularly polarized laser pulses create a unique situation where the optical fields at the tip surface are largely reduced while keeping the deposited energy inside the tip nearly the same as in the case of the linear polarization. This situation can be used to distinguish the two emission mechanisms mentioned above, because the signal levels of rescattering emission depend on the optical fields at *the surface* of the tip apex [19,24], while the thermal emission depends on the deposited thermal energy, or the optical fields *inside* the tip [16,17].

To support this argument, we simulated field distributions outside and inside the tip for linear and circular (left-handed) polarizations with the same energy flux and show them in Figs. 5(a) and 5(b), respectively. Here, we show a time average of moduli of field vectors. They are cross-sectional views on the $x-z$ plane. Although these distributions are similar to each other, a striking difference can be found between fields inside and outside of the tip. For Fig. 5(c), we plotted line profiles of fields along the white line in Figs. 5(a) and 5(b). The white lines intersect the emission sites where we measured the energy spectra. These line profiles show that the optical

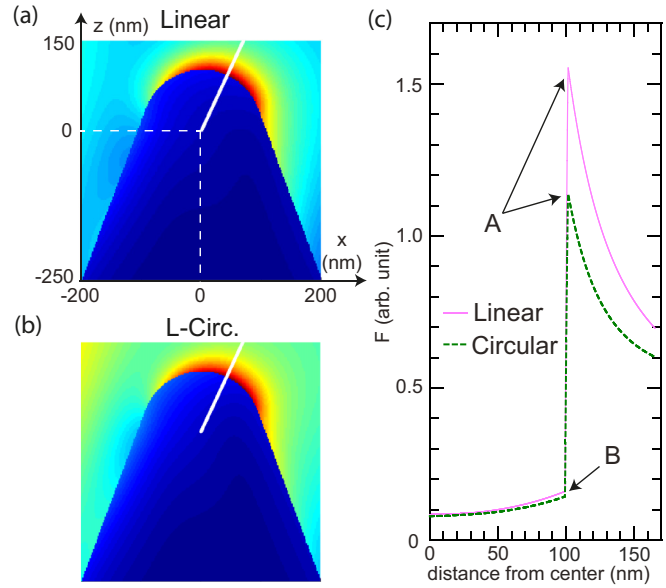

FIG. 5. The cross-sectional view of the calculated time-averaged field distribution on the $x-y$ plane for (a) linearly and (b) left-handed circularly polarized light. (c) Line profiles of the electric fields along the white lines in (a,b), which start from the center of the hemispherical tip apex.

fields outside the tip largely drop while the field inside the tip remains almost the same between the linear (solid lines) and circular (dashed lines) polarizations. The absorbed energy in the tip is obtained by calculating the power density of resistive heating [16,46], which is given by $\sigma \times E^2$. Here σ is conductivity and E is the electric field inside the tip. Because the absorbed energy is proportional to the square of the electric field, we evaluated the intensity at the surface of the apex [point A in Fig. 5(c)] and inside the tip [point B in Fig. 5(c)] for both polarizations. In addition, we evaluated the total amount of absorbed energy in the tip by integrating the power density of resistive heating three dimensionally over the volume of the tip where its cross-sectional view is displayed in Figs. 5(a) and 5(b). The obtained values are normalized to the values for linear polarization for each case, and are summarized in Table II.

Table II shows that the intensity at the surface drops by around 55%, while the intensity inside the tip at point B and the total deposited energy change by only 10%–20% between the linear and circular polarizations. In the experimental observation, as discussed above, the count rates of the low-energy peaks for circular polarization are comparable with that of linear polarization with the fluence of

TABLE II. The intensities of optical fields at points A and B in Fig. 5(c) and total deposited energy in the tip for linearly and circularly polarized laser light. These values are normalized at the values of linearly polarized light.

	Linear	L-Circ.
F^2 at A	1	0.54
F^2 at B	1	0.80
Total deposited energy	1	0.89

$6.7\,\mathrm{mJ/cm^2}$, which is 55% with respect to the maximum fluence ($12.2\,\mathrm{mJ/cm^2}$). If we assume that the low-energy peak originates from the delayed emission via the inelastic rescattering process, this observation is consistent with the 55% intensity reduction at the surface in our simulation. In contrast, if the low-energy peak is due to thermal emission, its signal level for circular polarization would remain similar to that of linear polarization for the same fluence, which is not the case in our observation. Therefore, our current observation and simulations support our previous conclusion where the rescattering process drives the delayed emission.

IV. CONCLUSION

We have investigated emission patterns and energy spectra driven by circularly polarized laser pulses. The emission patterns change depending on the helicity, which are driven by the different propagation directions of the excited surface electromagnetic waves. These results indicate that the use of circular polarization adds further knobs to control the site-selective ultrafast electron emission on the nanoscale. One application might be as a subcycle optical switch. Furthermore, the asymmetric emission could be used to characterize the helicity of the laser. The electron dynamics in the strong-field regime were also discussed by comparing energy spectra for circular and linear polarizations. The measured energy spectra for circular polarization showed the low-energy peak and plateau features, which were also observed for linearly polarized light. The plasmonic simulations revealed that circular polarization behaves almost like linear polarization on the tip surface. This implies that laser-induced electron dynamics should be the same as those under linear polarization, which is consistent with what we observed. Also, the plasmonic simulations reveal that circular polarization creates a unique situation with respect to linear polarization, where the optical fields at the tip surface are nearly halved while maintaining almost the same level of energy deposited into the apex. This unique situation distinguishes the phenomena due to strong-field effects at the surface and thermal effects, and thus the measured spectra corroborate our earlier conclusion that the low-energy peak feature is due to the strong-field effects at the surface.

ACKNOWLEDGMENTS

This work was supported by the Swiss National Science Foundation through the Ambizione (Grant No. PZ00P2_-131701) and the NCCR MUST; the Kazato Research Foundation; the Murata Science Foundation; the Sumitomo Foundation; the Research Foundation for Opto-Science and Technology; the Japanese Science and Technology Agency via the PRESTO project (Grant No. 1082208); the PETACom project financed by FET Open H2020 program; the Deutsche Forschungsgemeinschaft (DFG, German Research Foundation) via DFG project funding (Project No. 389759512), SPP1840; and the EU via ATTOCO Grant No. 307203).

[1] M. Aeschlimann, M. Bauer, D. Bayer, T. Brixner, F. J. García de Abajo, W. Pfeiffer, M. Rohmer, C. Spindler, and F. Steeb, Nature **446**, 301 (2007).
[2] A. Schiffrin, T. Paasch-Colberg, N. Karpowicz, V. Apalkov, D. Gerster, S. Muehlbrandt, M. Korbman, J. Reichert, M. Schultze, S. Holzner, J. V. Barth, R. Kienberger, R. Ernstorfer, V. S. Yakovlev, M. I. Stockman, and F. Krausz, Nature **493**, 70 (2013).
[3] P. Dombi, A. Hörl, P. Racz, I. Marton, A. Trügler, J. R. Krenn, and U. Hohenester, Nano Lett. **13**, 674 (2013).
[4] R. G. Hobbs, Y. Yang, A. Fallahi, P. D. Keathley, E. D. Leo, F. X. Kärtner, W. S. Graves, and K. K. Berggren, ACS Nano **8**, 11474 (2014).
[5] R. G. Hobbs, W. P. Putnam, A. Fallahi, Y. Yang, F. X. Kärtner, and K. K. Berggren, Nano Lett. **17**, 6069 (2017).
[6] P. Hommelhoff, Y. Sortais, A. Aghajani-Talesh, and M. A. Kasevich, Phys. Rev. Lett. **96**, 077401 (2006).
[7] H. Yanagisawa, C. Hafner, P. Dona, M. Klöckner, D. Leuenberger, T. Greber, M. Hengsberger, and J. Osterwalder, Phys. Rev. Lett. **103**, 257603 (2009).
[8] H. Yanagisawa, C. Hafner, P. Dona, M. Klöckner, D. Leuenberger, T. Greber, J. Osterwalder, and M. Hengsberger, Phys. Rev. B **81**, 115429 (2010).
[9] H. Yanagisawa, Ann. Phys. **525**, 126 (2012).
[10] H. Yanagisawa, M. Ciappina, C. Hafner, J. Schoetz, J. Osterwalder, and M. F. Kling, Sci. Rep. **7**, 12661 (2017).
[11] D. Ehberger, J. Hammer, M. Eisele, M. Krüger, J. Noe, A. Högele, and P. Hommelhoff, Phys. Rev. Lett. **114**, 227601 (2015).
[12] C. Ropers, D. R. Solli, C. P. Schulz, C. Lienau, and T. Elsaesser, Phys. Rev. Lett. **98**, 043907 (2007).
[13] B. Barwick, C. Corder, J. Strohaber, N. Chandler-Smith, C. Uiterwaal, and H. Batelaan, New J. Phys. **9**, 142 (2007).
[14] L. Wu and L. K. Ang, Phys. Rev. B **78**, 224112 (2008).
[15] H. Yanagisawa, M. Hengsberger, D. Leuenberger, M. Klöckner, C. Hafner, T. Greber, and J. Osterwalder, Phys. Rev. Lett. **107**, 087601 (2011).
[16] C. Kealhofer, S. M. Foreman, S. Gerlich, and M. A. Kasevich, Phys. Rev. B **86**, 035405 (2012).
[17] H. Yanagisawa, V. Zadin, K. Kunze, C. Hafner, A. Aabloo, D. Kim, M. F. Kling, F. Djurabekova, J. Osterwalder, and W. Wuensch, APL Photonics **1**, 091305 (2016).
[18] P. Hommelhoff, C. Kealhofer, and M. A. Kasevich, Phys. Rev. Lett. **97**, 247402 (2006).
[19] M. Krueger, J. Hammer, M. Eisele, M. Kruger, J. Noe, A. Hogele, and P. Hommelhoff, Nature (London, UK) **475**, 78 (2011).
[20] G. Herink, D. R. Solli, M. Gulde, and C. Ropers, Nature (London, UK) **483**, 190 (2012).
[21] M. Pant and L. K. Ang, Phys. Rev. B **86**, 045423 (2012).
[22] L. Wimmer, G. Herink, D. R. Solli, S. V. Yalunin, K. E. Echternkamp, and C. Ropers, Nat. Phys. **10**, 432 (2014).

[23] M. E. Swanwick, P. D. Keathley, A. Fallahi, P. R. Krogen, G. Laurent, J. Moses, F. X. Kärtner, and L. F. Velásquez-García, Nano Lett. **14**, 5035 (2014).
[24] H. Yanagisawa, S. Schnepp, C. Hafner, M. Hengsberger, D. Kim, M. F. Kling, A. Landsman, L. Gallmann, and J. Osterwalder, Sci. Rep. **6**, 35877 (2016).
[25] B. Forg, J. Schötz, F. Süßmann, M. Förster, M. Krüger, B. Ahn, W. A. Okell, K. Wintersperger, S. Zherebtsov, A. Guggenmos, V. Pervak, A. Kessel, S. A. Trushin, A. M. Azzeer, M. I. Stockman, D. Kim, F. Krausz, P. Hommelhoff, and M. F. KlingNat. Commun. **7**, 11717 (2016).
[26] D. Hoff, M. Krüger, L. Maisenbacher, A. M. Sayler, G. G. Paulus, and P. Hommelhoff, Nat. Phys. **13**, 947 (2017).
[27] B. Ahn, J. Schötz, M. Kang, W. Okell, S. Mitra, B. Förg, S. Zherebtsov, F. Süßmann, C. Burger, M. Kübel, C. Liu, A. Wirth, E. Fabrizio, H. Yanagisawa, D. Kim, B. Kim, and M. F. Kling, APL Photon. **2**, 036104 (2017).
[28] J. Schotz, S. Mitra, H. Fuest, M. Neuhaus, W. A. Okell, M. Forster, T. Paschen, M. F. Ciappina, H. Yanagisawa, P. Wnuk, P. Hommelhoff, and M. F. Kling, Phys. Rev. A **97**, 013413 (2018).
[29] C. Li, K. Chen, M. Guan, X. Wang, X. Zhou, F. Zhai, J. Dai, Z. Li, Z. Sun, S. Meng, K. Liu, and Q. Dai, Nat. Commun. **10**, 4891 (2019).
[30] R. Gomer, *Field Emission and Field Ionization* (American Institute of Physics, New York, 1993).
[31] A. Tonomura, Proc. Natl. Acad. Sci. USA **102**, 14952 (2005).
[32] J-N. Longchamp, S. Rauschenbach, S. Abb, C. Escher, T. Latychevskaia, K. Kern, and H-W. Fink, Proc. Natl. Acad. Sci. USA **114**, 1474 (2017).
[33] J-W. Han, J. S. Oh, and M. Meyyappan, App. Phys. Lett. **100**, 213505 (2012).
[34] M. Mueller, A. Paarmann, and R. Ernstorfer, Nat. Commun. **5**, 5292 (2014).
[35] M. Gulde, S. Schweda, G. Storeck, M. Maiti, H. K. Yu, A. M. Wodtke, S. Schäfer, and C. Ropers, Science, **345**, 200 (2014).
[36] T. Higuchi, L. Maisenbacher, A. Liehl, P. Dombi, and P. Hommelhoff, App. Phys. Lett. **106**, 051109 (2015).
[37] A. H. Firester, M. H. Heller, and P. Sheng, Appl. Opt. **16**, 1971 (1977).
[38] M. Sato, Phys. Rev. Lett. **45**, 1856 (1980).
[39] C. Hafner, OPENMAXWELL, http://openmax.ethz.ch/ (2014), accessed 12 August, 2019.
[40] *CRC Handbook of Chemistry and Physics*, 90th ed., edited by D. R. Lide (CRC Press, Boca Raton, FL, 2009).
[41] G. R. Fowles, *Introduction to Modern Optics* (Dover Publications Inc., New York, 1990).
[42] F. Yang, J. R. Sambles, and G. W. Bradberry, Phys. Rev. B **44**, 5855 (1991).
[43] See Supplemental Material at http://link.aps.org/supplemental/10.1103/PhysRevB.101.045406 for the temporal evolution of local electric field distributions for one optical cycle.
[44] A. N. Pfeiffer, C. Cirelli, M. Smolarski, D. Dimitrovski, M. Abu-samha, L. B. Madsen, and U. Keller, Nat. Phys. **8**, 76 (2012).
[45] W. Becker, S. P. Goreslavski, D. B. Milosevic, and G. G. Paulus, J. Phys. B: At., Mol. Opt. Phys. **51**, 162002 (2018).
[46] J. D. Jackson, *Classical Electrodynamics*, 3rd ed. (Wiley, New York, 1998).